

Transient Stability Analysis of Converter-based Islanded Microgrids Based on Iterative Equal Area Criterion Considering Reactive Power Loop Dynamics and Varying Damping

Xilin Li, *Student Member, IEEE*, Jingyi Zhang, Zhen Tian, *Member, IEEE*, Xiaoming Zha, *Senior Member, IEEE*, Wei Wang, Meng Huang, *Member, IEEE*, and Chong Shao

Abstract—With the rapid increase in the installed capacity of renewable energy in modern power systems, the stable operation of power systems with considerable power electronic equipment requires further investigation. In converter-based islanded microgrid (CIM) systems equipped with grid-following (GFL) and grid-forming (GFM) voltage-source converters (VSCs), it is challenging to maintain stability due to the mutual coupling effects between different VSCs and the loss of voltage and frequency support from the power system. In previous studies, quantitative transient stability analysis was primarily used to assess the active power loop of GFM-VSCs. However, frequency and voltage dynamics are found to be strongly coupled, which strongly affects the estimation result of stability boundary. In addition, the varying damping terms have not been fully captured. To bridge these gaps, this paper investigates the transient stability of CIM considering reactive power loop dynamics and varying damping. First, an accuracy-enhanced nonlinear model of the CIM is derived based on the effects of reactive power loop and post-disturbance frequency jump phenomena. Considering these effects will eliminate the risk of misjudgment. The reactive power loop dynamics make the model coefficients be no longer constant and thus vary with the power angle. To evaluate quantitatively the effects of reactive power loop and varying damping on the transient stability of CIM, an iterative criterion based on the equal area criterion theory is proposed. In addition, the effects of parameters on the stable boundary of power system are analyzed, and the dynamic interaction mechanisms are revealed. Simulation and experiment results verify the merits of the proposed method.

Index Terms—Transient stability, converter, iterative criterion, reactive power loop, post-disturbance frequency jump.

Manuscript received: May 6, 2023; revised: August 24, 2023; accepted: November 20, 2023. Date of CrossCheck: November 20, 2023. Date of online publication: December 12, 2023.

This work was supported in part by the National Key Research and Development Program of China (No. 2022YFB2402700) and in part by the Science and Technology Project of State Grid Corporation of China (No. 52272222001J).

This article is distributed under the terms of the Creative Commons Attribution 4.0 International License (<http://creativecommons.org/licenses/by/4.0/>).

X. Li, J. Zhang, Z. Tian, X. Zha (corresponding author), and M. Huang are with Hubei Key Laboratory of Power Equipment & System Security for Integrated Energy, School of Electrical Engineering and Automation, Wuhan University, Wuhan, China (e-mail: snplee@whu.edu.cn; zhjydyx@126.com; ztian.lee@whu.edu.cn; xmzha@whu.edu.cn; meng.huang@whu.edu.cn).

W. Wang is with the NARI Technology Co., Ltd., Nanjing, China (e-mail: wangwei@sgepri.sgcc.com.cn).

C. Shao is with State Grid Gansu Electric Power Company, Lanzhou, China (e-mail: shaochong@gs.sgcc.com.cn).

DOI: 10.35833/MPCE.2023.000291

I. INTRODUCTION

THE penetration of power electronic equipment implanted in modern power systems has been rapidly increasing [1]–[3]. The converter-based islanded microgrid (CIM) has the advantages of flexible operation and high efficiency, and is a promising way for renewable energy integration. However, the CIM may lead to new challenges for the transient stability of power systems due to its low-inertial characteristics, the dynamic interactions between grid-tied converters (GTCs), and the loss of voltage and frequency support from the power system. The transient stability of the CIM is urgently required for analysis. GTCs dominate the stability of the CIM [4], [5]. Based on different voltage/frequency generation mechanisms, GTCs are classified as grid-forming (GFM) or grid-following (GFL) voltage-source converters (VSCs). Reference [6] proposes that a GFL-VSC could be equivalent to a controlled current source parallel to high impedance. By contrast, a GFM-VSC could be equivalent to a controlled voltage source in series with high conductance. GFM control includes droop control, power synchronization control, virtual oscillator control, and virtual synchronous generator (VSG) control [5], [7]–[9]. GFM-VSCs can construct their own AC-side output voltage without relying on an external AC system. Therefore, GFM-VSCs can operate in isolation or be connected to extremely weak grids [10], [11]. GFM-VSCs show excellent advantages in terms of stability support by providing virtual inertia and good robustness to weak grids. However, GFM-VSCs face the challenge of a limited overcurrent capacity. GFL-VSCs are mainly controlled by a phase-locked loop (PLL), DC-link voltage loop, and inner current controller. Their output voltage is determined by the current reference and grid parameters [12]–[14]. GFL-VSCs can achieve the maximum power tracking [15] and high power-factor operations. The external characteristics of the current source provide the advantage of limiting the fault current. In addition, GFL-VSCs have the advantage of fast response. However, GFL-VSCs require an external grid to provide the voltage and frequency as inputs. Therefore, GFL-VSCs are prone to synchronization instabilities under unstable grid voltages and frequencies. GFL-

VSCs cannot be used alone in weak or isolated microgrids with high renewable-energy penetration rates. As a result, a practical CIM should include both types of converters: GFM-VSCs that provide voltage/frequency support and GFL-VSCs that provide fast power response [16].

The transient stability of GTCs has been evaluated using several methods. The Lyapunov [17]-[21] and Hamilton [4], [22] methods have complete theoretical frameworks, but the results are too conservative. Phase-portrait methods [23], [24] fail to derive analytical criteria. The equal area criterion (EAC) is intuitive for second-order systems and has strong physical significance [5], [25]-[29].

The difficulty in the transient stability analysis of GFL-VSCs mainly lies in accurately estimating the adverse effects caused by nonlinear varying damping, which brings significant conservatism to the stability criteria. The damping term of the GFL-VSC changes with the system power angle. When the power angle exceeds 90° , the damping exhibits negative characteristics and causes stability to deteriorate. As a result, stability misjudgment occurs when negative damping is ignored, as in the conventional EAC method proposed in [25]. In [21] and [22], a subset of stability within the positive damping interval is regarded as the stable domain estimation, but with relatively high conservatism since the negative damping region is directly aborted. In [5], an improved EAC method is proposed to quantify the adverse effects of negative damping of the PLL on system stability. However, the improved EAC method is unavoidably conservative due to the mathematical inequality derived from varying damping. In [17], a new Lyapunov direct method is proposed with an enlarged dissipation region and partially improved conservatism as compared with [21], [22]. However, the physical significance of the proposed Lyapunov function (LF) is unclear. In addition, a post-disturbance frequency jump phenomenon occurs in the PLL at the disturbed moment due to the proportional control, which is detrimental to the transient stability of the PLL. However, nearly all previous studies on PLL have been based on the second-order simplified oscillation model proposed in [25], which is similar to that of a synchronous generator. This model does not consider the aforementioned abrupt frequency change phenomenon. In other words, the instantaneous frequency at the moment of disturbance is assumed to be zero, which may lead to stability misjudgment. In [30], a nearly conservatism-free transient stability assessment method is proposed for a single GFL-VSC connected to an infinite power system. However, it does not consider the potential dynamic interaction between the GFL-VSC and grid (noninfinite grid) or other converters that may exist in the system. The system analyzed in [30] is too simplistic and idealistic, showing little practical value. By contrast, the CIM system considered in this paper conforms to the future development trend of renewable energy generation systems, as it is a 100% converter-based system and thus has strong engineering guiding significance.

The difficulties in evaluating the transient synchronization stability of GFM-VSCs are primarily the coupling effects between the active and reactive power loops [24], [31]-[33], which deteriorate stability due to the decrease in voltage.

Reference [24] analyzes this unfavorable coupling in droop-VSC using a phase portrait method rather than an analytic criterion but fails to reveal the instability mechanism. A GFM-VSC model that considers the reactive power loop has been established in [32] and used to derive the attraction domain of the GFM-VSC using the Takagi-Sugeno (T-S) method. However, the accuracy of the stable boundary is questionable because of its high conservatism. In [33], the effects of a reactive power loop based on a quasi-steady model are investigated. However, the proposed criterion requires numerical integration. The aforementioned study regards VSG output voltage E as a parameter in the LF instead of directly substituting the quasi-steady-state function of E about δ into LF. Therefore, the value of E must be renewed in real time through numerical integration. This may be explained by the fact that the substitution of $E(\delta)$ makes it difficult to prove the positive definite of LF or the semi-negative definite of the LF derivative.

The existing literature has seldom investigated the transient stability of CIM systems under the interaction of different types of converters. In addition to the respective difficulties of the GFM-VSC and GFL-VSC previously mentioned, the analytical difficulties of transient stability in CIM systems include analysis of the dynamic interactions between different types of converters [4], [5]. In [34], a model of a mixed-GFM-GFL-based CIM system is established but a quantitative criterion is not provided. Reference [16] indicates that adding GFM-VSCs to a PLL-integrated system is beneficial for stability. However, it is based only on a small-signal stability analysis method. In [4], a Hamilton-based transient criterion is proposed for the aforementioned CIM system, but the negative damping interval is aborted directly, which is too conservative. In [5], the effects of PLL negative damping are partially considered, which improves the conservatism to some extent. However, it does not consider the effects of the GFM-VSC reactive power loop.

In this paper, an accuracy-enhanced model and iterative EAC are proposed to derive the transient stable domain of the CIM more accurately, as this enables full capture of the positive and negative damping effects, reactive power loop, and abrupt frequency change phenomenon. The contributions of this paper can be summarized as follows.

- 1) Considering the effects of the reactive power loop and the abrupt frequency changes that exist in both GFL-VSCs and GFM-VSCs, an accuracy-enhanced model of the CIM is derived, which eliminates the risk of stability misjudgment. Further derivation shows that the stability of the CIM system differs under different perturbation forms.

- 2) An iterative EAC method is proposed for accurate estimation of the stable boundaries in which the nonlinear varying damping and reactive power loop are fully captured. The proposed method is verified to be considerably more accurate than existing methods.

- 3) The physical mechanism by which the interaction between two VSCs worsens or enhances system stability is quantified.

The remainder of this paper is organized as follows. Section II describes the nonlinear modeling of a CIM system

that includes both a GFL-VSC and GFM-VSC. Section III proposes an iterative EAC for stable domain estimation, which is free of conservatism and fully captures the dynamics of nonlinear damping and the reactive power control loop. In Section IV, the interaction mechanisms between two converters are revealed and the effects of different parameters on the stable domain are visualized. Section V shows simulation and experimental verification of the accuracy-enhanced nonlinear model of CIM. Section VI provides further discussion on future work, demonstrating the strong extensibility of the proposed method. Section VII concludes this paper.

II. NONLINEAR MODELING OF CIM SYSTEM

Figure 1(a) shows the overall structure of the CIM system, with several GFL-VSCs and GFM-VSCs parallel to the constant power load $P_{\text{Load}} + jQ_{\text{Load}}$. Considering that the converter parameters of the same control type in the same microgrid are similar (they do not have to be identical), they can be assumed to satisfy the homology criterion proposed in [35]. As a result, the CIM system presented in Fig. 1(a) can be simplified to that shown in Fig. 1(b) based on the Hamilton-action theory [35], [36].

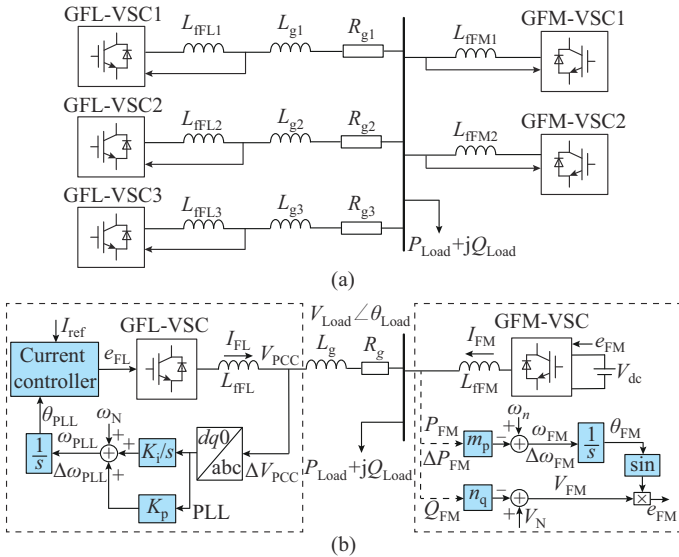


Fig. 1. Topological and control structure of a CIM system. (a) Detailed model of CIM system. (b) Simplified equivalent model and control diagram of CIM system.

This paper investigates the effects of the interaction between GFM-VSCs and GFL-VSCs on the transient stability of the CIM system. Therefore, only the simplified system shown in Fig. 1(b) is analyzed. Details on homogeneous equivalence are provided in our earlier paper [35] and are thus not repeated here. In Fig. 1, L_g and R_g are the line inductance and resistance, respectively; L_f is the output filter of the converter; subscripts FL and FM correspond to the GFL-VSC and GFM-VSC, respectively; and subscripts 1-3 correspond to the serial numbers of VSCs. The strategy for a PLL cascaded with a current controller is applied to a GFL-VSC, where K_p and K_i are the proportional and integral coefficients of PLL, respectively; V_{PCC} and θ_{PCC} are the voltage and phase at the point of common coupling (PCC), respectively; θ_{PLL} is the output phase

of the PLL; ω_{PLL} and ω_n are the output frequency of the PLL and the nominal frequency, respectively; and I_{ref} is the reference current. The GFM-VSC is controlled by a droop controller, where m_p and n_q are the active and reactive droop coefficients, respectively; P_{FM} and Q_{FM} are the active and reactive power of the GFM-VSC, respectively; ω_{FM} and θ_{FM} are the output frequency and phase of the droop controller, respectively; V_N and V_{FM} are the aptitudes of nominal and output voltage of the GFM-VSC, respectively; V_{Load} and θ_{Load} are the amplitude and phase of the load voltage, respectively; I_{FM} and I_{FL} are the output currents of the GFM-VSC and GFL-VSC, respectively; e_{FL} and e_{FM} are the pulse width modulation signals of the GFL-VSC and GFM-VSC, respectively; and V_{dc} is the voltage on the DC-side capacitor.

The dynamics of the inner current loop of the GFL-VSC are much faster than those of the PLL and thus have less impact on stability analysis. Therefore, the dq -axis components of the output currents of GFL-VSC, i.e., $I_{\text{FL}d}$ and $I_{\text{FL}q}$, can be assumed to be equal to the reference values $I_{\text{ref}d}$ and $I_{\text{ref}q}$, respectively.

$$\begin{cases} I_{\text{FL}d} = I_{\text{ref}d} = I_{\text{ref}} \cos \varphi \\ I_{\text{FL}q} = I_{\text{ref}q} = I_{\text{ref}} \sin \varphi \end{cases} \quad (1)$$

where φ is the power factor angle of the GFL-VSC. According to the structure of the simplified CIM model presented in Fig. 1(b), V_{PCC} can be derived as:

$$\begin{aligned} V_{\text{PCC}} \angle \theta_{\text{PCC}} &= V_{\text{Load}} \angle \theta_{\text{Load}} + R_g I_{\text{ref}} \angle (\theta_{\text{PLL}} + \varphi) + \\ &L_g \frac{d}{dt} [I_{\text{ref}} \angle (\theta_{\text{PLL}} + \varphi)] \end{aligned} \quad (2)$$

Applying Park transformation with the reference phase θ_{PLL} on (2), the following equation can be derived:

$$\begin{cases} V_{\text{PCC}d} = V_{\text{Load}} \cos(\theta_{\text{Load}} - \theta_{\text{PLL}}) + I_{\text{ref}} R_g \cos \varphi - \omega_{\text{PLL}} L_g I_{\text{ref}} \sin \varphi \\ V_{\text{PCC}q} = V_{\text{Load}} \sin(\theta_{\text{Load}} - \theta_{\text{PLL}}) + I_{\text{ref}} R_g \sin \varphi + \omega_{\text{PLL}} L_g I_{\text{ref}} \cos \varphi \end{cases} \quad (3)$$

where $V_{\text{PCC}d}$ and $V_{\text{PCC}q}$ are the dq -axis components of V_{PCC} . Based on the PLL structure shown in Fig. 1(b), the dynamics can be expressed as:

$$\theta_{\text{PLL}} = \int_0^t \left(K_p V_{\text{PCC}q} + K_i \int_0^t V_{\text{PCC}q} \tau + \omega_n \right) d\tau \quad (4)$$

Ignoring the fast dynamics of the inner loops of the GFM-VSC, we obtain:

$$\begin{cases} \theta_{\text{FM}} \approx \theta_{\text{Load}} \\ \omega_{\text{FM}} \approx \omega_{\text{Load}} \\ V_{\text{FM}} \approx V_{\text{Load}} \end{cases} \quad (5)$$

where ω_{Load} is the time derivative of θ_{Load} . We next define $\delta = \theta_{\text{PLL}} - \theta_{\text{Load}}$ as the virtual power angle of the CIM system. Then, by combining (1)-(5), we can obtain:

$$\begin{cases} \dot{\delta} = \omega_{\text{PLL}} - \omega_{\text{Load}} = \omega \\ M \dot{\omega} = -K_i V_{\text{Load}} \sin \delta + K_i I_{\text{ref}} R_g \sin \varphi + \\ \quad (\omega + \omega_{\text{Load}}) K_i L_g I_{\text{ref}} \cos \varphi - \\ \quad K_p V_{\text{Load}} \omega \cos \delta + K_p \dot{\omega}_{\text{Load}} L_g I_{\text{ref}} \cos \varphi - \dot{\omega}_{\text{Load}} \\ M = 1 - K_p L_g I_{\text{ref}} \cos \varphi \end{cases} \quad (6)$$

where ω is the time derivative of δ ; and M is the equivalent

inertia. The active power P_{FL} and reactive power Q_{FL} generated by the GFL-VSC can be derived as:

$$\begin{cases} P_{\text{FL}} = 1.5V_{\text{PCCd}}I_{\text{ref}d} + 1.5V_{\text{PCCq}}I_{\text{ref}q} = \\ \quad 1.5V_{\text{Load}}I_{\text{ref}} \cos(\delta + \varphi) + 1.5I_{\text{ref}}^2 R_{\text{g}} \\ Q_{\text{FL}} = 1.5V_{\text{PCCq}}I_{\text{ref}d} - 1.5V_{\text{PCCd}}I_{\text{ref}q} = \\ \quad -1.5V_{\text{Load}}I_{\text{ref}} \sin(\delta + \varphi) + 1.5\omega_{\text{PLL}}L_{\text{g}}I_{\text{ref}}^2 \end{cases} \quad (7)$$

The active power consumed by the line as P_{g} and the reactive power consumed by the line as Q_{g} , are given by:

$$\begin{cases} P_{\text{g}} = 1.5I_{\text{ref}}^2 R_{\text{g}} \\ Q_{\text{g}} = 1.5I_{\text{ref}}^2 L_{\text{g}}\omega_{\text{PLL}} \end{cases} \quad (8)$$

Therefore, the output active power P_{FM} and reactive power Q_{FM} of the GFM-VSC can be derived as:

$$\begin{cases} P_{\text{FM}} = P_{\text{Load}} + P_{\text{g}} - P_{\text{FL}} = P_{\text{Load}} - 1.5V_{\text{Load}}I_{\text{ref}} \cos(\delta + \varphi) \\ Q_{\text{FM}} = Q_{\text{Load}} + Q_{\text{g}} - Q_{\text{FL}} = Q_{\text{Load}} + 1.5V_{\text{Load}}I_{\text{ref}} \sin(\delta + \varphi) \end{cases} \quad (9)$$

According to the P - ω active droop and Q - V reactive droop controller structure shown in Fig. 1(b), the output frequency ω_{FM} and output voltage V_{FM} of the GFM-VSC can be derived as:

$$\omega_{\text{FM}} = \omega_n - m_{\text{p}}P_{\text{FM}} = \omega_n - m_{\text{p}}P_{\text{Load}} + 1.5m_{\text{p}}V_{\text{Load}}I_{\text{ref}} \cos(\delta + \varphi) \quad (10)$$

$$V_{\text{FM}}(\delta) = V_{\text{N}} - n_{\text{q}}Q_{\text{FM}} = \frac{V_{\text{N}} - n_{\text{q}}Q_{\text{Load}}}{1 + 1.5n_{\text{q}}I_{\text{ref}} \sin(\delta + \varphi)} \quad (11)$$

Combining (5), (6), (10), and (11), we can derive the CIM system model as:

$$\begin{cases} \dot{\delta} = \omega_{\text{PLL}} - \omega_{\text{FM}} = \omega \\ \dot{\omega} = k_1 - (k_2(\delta) \sin \delta + k_3(\delta) \cos \delta) - \\ \quad (k_4 + k_5(\delta) \cos \delta + k_6(\delta) \sin \delta) \omega \\ \dot{\delta}(t_{0+}) = \Delta \omega \end{cases} \quad (12)$$

where k_1 is the equivalent mechanical power; $k_2 \sin \delta + k_3 \cos \delta$ is the equivalent electromagnetic power; $k_4 + k_5(\delta) \cos \delta + k_6(\delta) \sin \delta$ is the equivalent nonlinear damping D_{eq} ; and $\Delta \omega$ is the value of the post-disturbance frequency jump in the CIM system, which is caused by the PLL and P - ω droop controller at the disturbed moment t_{0+} . Detailed expressions for M and k_1 - k_6 are given as:

$$\begin{cases} M = 1 - K_{\text{p}}L_{\text{g}}I_{\text{ref}} \cos \varphi \\ k_1 = \left[K_{\text{i}}I_{\text{ref}}R_{\text{g}} \sin \varphi + K_{\text{i}}L_{\text{g}}I_{\text{ref}} \cos \varphi (\omega_n - m_{\text{p}}P_{\text{Load}}) \right] / M \\ k_2(\delta) = K_{\text{i}}V_{\text{FM}}(\delta) (1 + 1.5m_{\text{p}}I_{\text{ref}}^2L_{\text{g}} \cos \varphi \sin \varphi) / M \\ k_3(\delta) = -1.5m_{\text{p}}V_{\text{FM}}(\delta)I_{\text{ref}}^2K_{\text{i}}L_{\text{g}} \cos^2 \varphi / M \\ k_4 = -K_{\text{i}}L_{\text{g}}I_{\text{ref}} \cos \varphi / M \\ k_5(\delta) = \left[K_{\text{p}}V_{\text{FM}}(\delta) (1 + 1.5m_{\text{p}}L_{\text{g}}I_{\text{ref}}^2 \cos \varphi \sin \varphi) - \right. \\ \quad \left. 1.5m_{\text{p}}V_{\text{FM}}(\delta)I_{\text{ref}} \sin \varphi \right] / M \\ k_6(\delta) = -1.5m_{\text{p}}V_{\text{FM}}(\delta)I_{\text{ref}} \cos \varphi \end{cases} \quad (13)$$

The variations in ω_{PLL} are always proportional to V_{PCCq} due to the proportional controller of PLL. When the system

encounters large disturbances, both V_{PCCq} and ω_{PLL} exhibit abrupt changes. This phenomenon, which occurs at the perturbed moment in the PLL, is defined as the frequency abrupt change of PLL $\Delta\omega_{\text{PLL}}$. In addition, the P - ω droop controller also experiences an abrupt change $\Delta\omega_{\text{FM}}$, which is caused by the abrupt change in active power distribution. A detailed expression of $\Delta\omega$ can be derived as:

$$\Delta\omega = \Delta\omega_{\text{PLL}} - \Delta\omega_{\text{Load}} = K_{\text{p}}\Delta V_{\text{PCCq}} - \Delta\omega_{\text{FM}} \quad (14)$$

where ΔV_{PCCq} and $\Delta\omega_{\text{FM}}$ can be expressed as:

$$\begin{aligned} \Delta V_{\text{PCCq}} \approx & -(V_{\text{FM}+} \sin(\delta_+) - V_{\text{FM}-} \sin(\delta_-)) + \\ & (\Delta\omega + \omega_{\text{FM}+})L_{\text{g}+}I_{\text{ref}+} \cos \varphi_+ - \omega_{\text{FM}-}L_{\text{g}-}I_{\text{ref}-} \cos \varphi_- + \\ & R_{\text{g}+}I_{\text{ref}+} \sin \varphi_+ - R_{\text{g}-}I_{\text{ref}-} \sin \varphi_- \end{aligned} \quad (15)$$

$$\begin{aligned} \Delta\omega_{\text{FM}} = \omega_{\text{FM}+} - \omega_{\text{FM}-} = & 1.5m_{\text{p}}(V_{\text{FM}+}I_{\text{ref}+} \cos(\delta_+ + \varphi_+) - \\ & V_{\text{FM}-}I_{\text{ref}-} \cos(\delta_- + \varphi_-)) - m_{\text{p}}(P_{\text{Load}+} - P_{\text{Load}-}) \end{aligned} \quad (16)$$

where the subscripts “+” and “-” distinguish the post- and pre-perturbation parameters, respectively. Compared with the existing models expressed in [4] and [5], the proposed model as derived from (12) innovatively captures both the reactive power loop dynamics and post-disturbance frequency jump phenomenon. In [4] and [5], the Q - V droop is ignored by assuming $V_{\text{FM}} \approx V_{\text{N}}$. Besides, the post-disturbance frequency jump is also ignored by assuming $\dot{\delta}(t_{0+}) = 0$. Figure 2 shows a simulation comparison between the existing models derived from [4] and [5] and the proposed model as formulated in (12). Table I lists the parameters of the CIM analyzed in this paper, where K_{pC} and K_{iC} are the parameters of the current loop. All of the three-phase voltage and current variables refer to the amplitudes of the instantaneous values of the phase voltage/current. The maximum power angle error and maximum frequency error as given in (12) are only 6% and 3% of those of the existing model under the perturbation shown in Fig. 2(a) and (b), respectively.

In addition to improving the model accuracy, the improvement derived from (12) can also avoid the misjudgment of system stability, as shown in Fig. 2(c) and (d). This misjudgment may occur in the existing model [4], [5] when the effects of the post-disturbance frequency jump and reactive power loop are ignored. This is because the droop characteristic of the reactive power loop in (11) causes a decrease in output voltage of the GFM-VSC, which results in reduced electromagnetic power and stability. The post-disturbance frequency jump is equivalent to generating a certain amount of initial kinetic energy, which further deteriorates stability. Misinterpreting unstable systems as stable is unacceptable in practical engineering. In previous studies, with the inevitable errors derived from stability analysis methods (where the effects of work done by the damping term cannot be accurately assessed), the stability boundary cannot be estimated accurately. Therefore, the misjudgment as depicted in Fig. 2(c) and (d) does not occur. For accurate evaluation of transient stability of the CIM, a stability criterion that is free of conservatism and fully considers nonlinear damping, the reactive power loop, and post-disturbance frequency jump phenomenon is proposed in Section III.

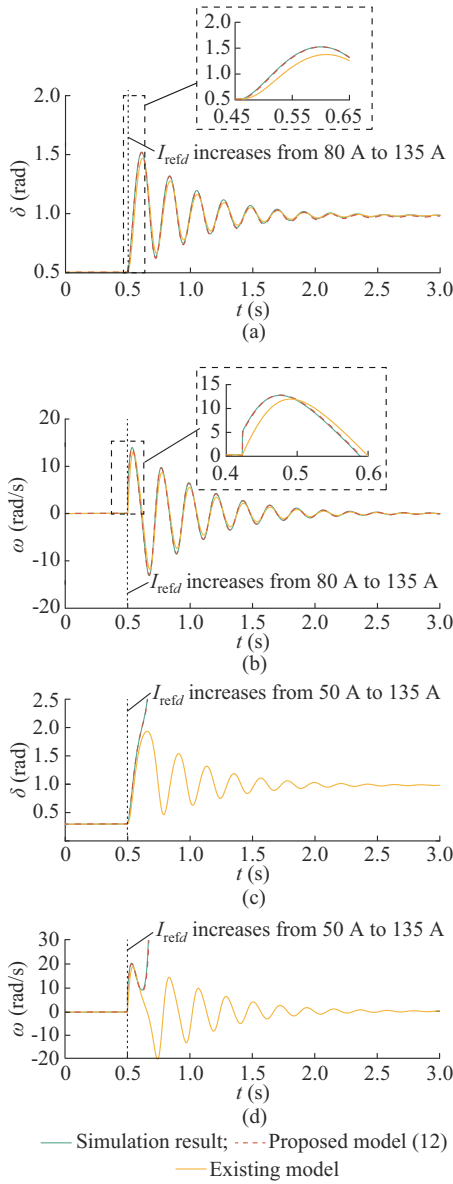


Fig. 2. Model comparison. (a) δ (stable). (b) ω (stable). (c) δ (unstable). (d) ω (unstable).

TABLE I
PARAMETERS OF CIM

Symbol	Value	Symbol	Value
K_{pC}, K_{iC}	5, 70	V_N	$110\sqrt{2}$ V
L_g	3 mH	m_p	10^{-5}
L_f	0.12 mH	ω_n	100π rad/s
n_q	10^{-4}	I_{refd}, I_{refiq}	135 A, 5 A
$P_{Load} + jQ_{Load}$	40 kW + j2 kvar	K_p, K_i	0.1, 10

III. PROPOSED ITERATIVE EAC

In the transient stability assessment of the CIM system as formulated in (12), the effects of varying damping D_{eq} and reactive power loop on the system are difficult to analyze quantitatively. The effect of D_{eq} must be fully captured, particularly in negative regions:

$$\delta > \delta_d = \arcsin\left(-k_4/\sqrt{k_5^2(\delta) + k_6^2(\delta)}\right) - \arctan(k_5(\delta)/k_6(\delta)) \quad (17)$$

This is because it imposes energy on the system and deteriorates stability [5]. In addition, the reactive power loop results in a smaller k_2 and further deteriorates stability. Without fully considering both the varying damping and reactive power loops, we cannot obtain an accurate and stable boundary estimation. However, the aforementioned difficulties can be overcome using the proposed method. With the iteration of the frequency ω and damping torque ωD_{eq} , the tedious nonlinear calculation in the time domain is skipped. The dynamic relationship between ω and δ can be directly obtained by using energy as an intermediary. The proposed method derives a transient stable boundary of the CIM system that is free of conservatism by fully considering the effects of the reactive power loop and varying damping but that does not require a time-domain numerical calculation.

A. Derivation of δ_{max}

Reference [37] shows that nonlinear damping, whether positive or negative, does not affect the upper stable boundary of system (12). As a result, the real upper boundary δ_{max} is exactly equal to the value estimated by the conventional EAC [25], i.e., δ_{maxC} , in which the damping term is not considered:

$$\begin{cases} k_1 - (k_2(\delta_{max})\sin\delta_{max} + k_3(\delta_{max})\cos\delta_{max}) = 0 \\ (k_2(\delta_{max})\sin\delta_{max} + k_3(\delta_{max})\cos\delta_{max})' < 0 \end{cases} \quad (18)$$

B. Derivation of $\omega(\delta)$

In (12), the energy conservation law is expressed as:

$$\frac{d(E_k + E_p - W_D)}{dt} = 0 \quad (19)$$

where E_k and E_p are the equivalent kinetic and potential energies of the CIM system, respectively; and W_D is the work performed by the varying damping term:

$$\begin{cases} E_k = \omega^2/2 \\ E_p = E_0 + \int (k_2(\delta)\sin\delta + k_3(\delta)\cos\delta - k_1) d\delta \\ W_D = - \int (k_4 + k_5(\delta)\cos\delta + k_6(\delta)\sin\delta) \omega(\delta) d\delta \end{cases} \quad (20)$$

where E_0 is the initial potential energy; and $\omega(\delta)$ is the frequency function that satisfies the process given in (12) under the varying damping terms $\omega(\delta)D_{eq}(\delta)$. Combining (19) and (20), the dynamic relationship between ω and δ can be revealed by the nonlinear implicit equation regarding $\omega(\delta)$:

$$\omega(x) = \sqrt{2 \int_x^{\delta_{max}} (k_2(\delta)\sin\delta + k_3(\delta)\cos\delta + D_{eq}(\delta)\omega(\delta) - k_1) d\delta} \quad (21)$$

where x is the lower power angle variable of the uncertain limit integral function. The varying damping and $Q-V$ droop controller dynamics are fully considered in (21). In addition, the accelerating and decelerating areas in (21) are shown as S_1 and $S_3 + S_4$ in Fig. 3, respectively. The conventional EAC

[25] neglects the works of both positive (S_2+S_3) and negative (S_5) damping and regards S_1+S_2 and S_4+S_5 as the accelerating and decelerating areas, respectively. Figure 3 also shows the post-disturbance frequency jump, denoted by the vertical line to the left of the solid blue curve. Section III-C provides details on the derivation of δ_{\min} considering the post-disturbance frequency jump. In Fig. 3, δ_e is the stable equilibrium point of system (12), and δ_d is the zero crossing point of damping, as shown in (17).

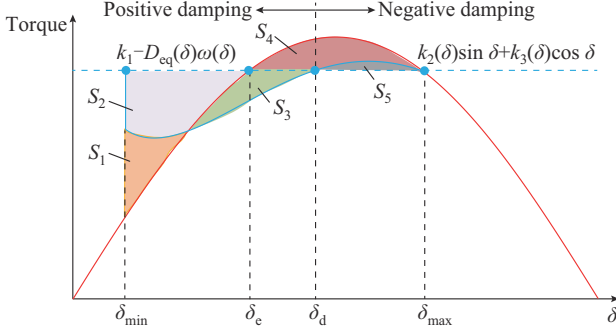


Fig. 3. EAC considering damping, reactive loop, and post-disturbance frequency jump.

The iterative EAC is proposed to solve implicit equation (21) iteratively. Figure 4 presents a flow of the iterative EAC. In the i^{th} iteration, the frequency function $\omega_i(\delta)$ is determined by the damping torque $D_{\text{eq}}(\delta)\omega_{i-1}(\delta)$ from the previous iteration by replacing $\omega(\delta)$ on the right side of (21) with $\omega_{i-1}(\delta)$:

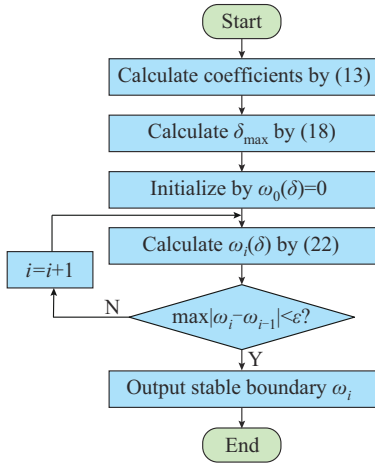


Fig. 4. Flow of iterative EAC.

$$\omega_i(x) = \sqrt{2 \int_x^{\delta_{\max}} (k_2(\delta) \sin \delta + k_3(\delta) \cos \delta - k_1 + D_{\text{eq}}(\delta) \omega_{i-1}(\delta)) d\delta} \quad (22)$$

The iteration is started by assuming $\omega_0(\delta) = 0$. When $\omega_i(\delta)$ converges to an acceptable range, the iterative calculation stops, and the derived $\omega_i(\delta)$ can be referred to as the frequency function $\omega(\delta)$ obtained by the proposed iterative EAC. To further facilitate understanding, a pseudocode is provided in Algorithm 1. It includes five main steps: ① pa-

parameter input; ② derivation of δ_{\max} ; ③ initialization of iteration; ④ iteration; and ⑤ stable boundary output. Algorithm 1 illustrates the engineering application steps of the proposed iterative EAC.

Algorithm 1: iterative EAC

```

Input  $V_n, I_{\text{ref}d}, I_{\text{ref}q}, P_{\text{Load}}, Q_{\text{Load}}, K_p, K_i, m_p, n_q, L_g, \omega_n$ 
% Input parameters
Define  $x = -\pi:10^{-5}:\pi$ 
Calculate  $k_1(x)-k_6(x)$  based on (13)
Calculate  $\delta_{\max}$  based on (18)
% Above is to derive  $\delta_{\max}$ 
Redefine  $x = -\pi:10^{-5}:\delta_{\max}$ 
Recalculate  $k_1(x)-k_6(x)$  based on (13)
Define  $\omega_0 = 0, i = 1$ 
% Above is initialization, below is iteration
While ( $|\omega_i(x) - \omega_{i-1}(x)| > \epsilon$  or  $i = 1$ )
    Calculate  $\omega_i(x)$  based on  $\omega_{i-1}(x)$ , by (22)
     $i++$ 
end
% Iteration is stopped, output stable boundary
Output  $\omega_i(x)$ 

```

Figure 5 shows the two negative convergence mechanisms of iteration described in Fig. 4. A larger $\omega_{i-1}(\delta)$ results in a more positive damping torque when D_{eq} is positive ($\delta < \delta_d$), which leads to a reduced accelerating area S_{acce} , and thus a smaller $\omega_i(\delta)$ is derived from (22). However, a larger $\omega(\delta)$ leads to a smaller damping torque when D_{eq} is negative ($\delta > \delta_d$), which results in a reduced decelerating area S_{deci} , and thus a smaller $\omega(\delta)$ is derived from (22), as $\omega(\delta_{\max}) = 0$.

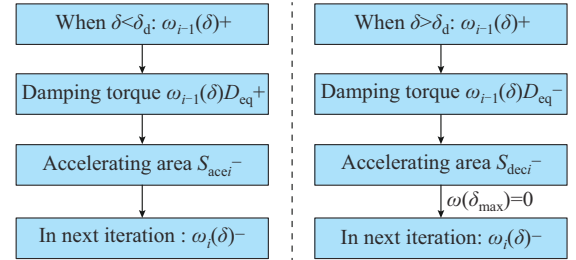


Fig. 5. Two negative convergence mechanisms of iteration.

Based on the iteration given in (22), only the $\omega > 0$ portion (right swing) of the stability boundary is obtained. To derive the complete stable boundary, a similar iteration as given in (23) could be applied to derive the $\omega < 0$ portion (left swing) of the stable boundary:

$$\omega_i(x) = -\sqrt{2 \int_x^{\delta_{\max}} (k_2(\delta) \sin \delta + k_3(\delta) \cos \delta - k_1 + D_{\text{eq}}(\delta) \omega_{i-1}(\delta)) d\delta} \quad (23)$$

C. Derivation of δ_{\min}

Considering the post-disturbance frequency jump indicated in (14) - (16), we can derive a frequency jump function $\Delta\omega_k(\delta)$. The input of $\Delta\omega_k(\delta)$ is the initial state of δ before the disturbance, and the output is the value of the post-disturbance frequency jump at the disturbed moment, where k denotes the perturbation. The frequency jump functions under

the current, voltage, inductance, and phase perturbation are denoted as $\Delta\omega_I(\delta)$, $\Delta\omega_V(\delta)$, $\Delta\omega_L(\delta)$, and $\Delta\omega_\theta(\delta)$, respectively, as shown in Fig. 6. The blue area represents the stable boundary obtained by (22) and (23).

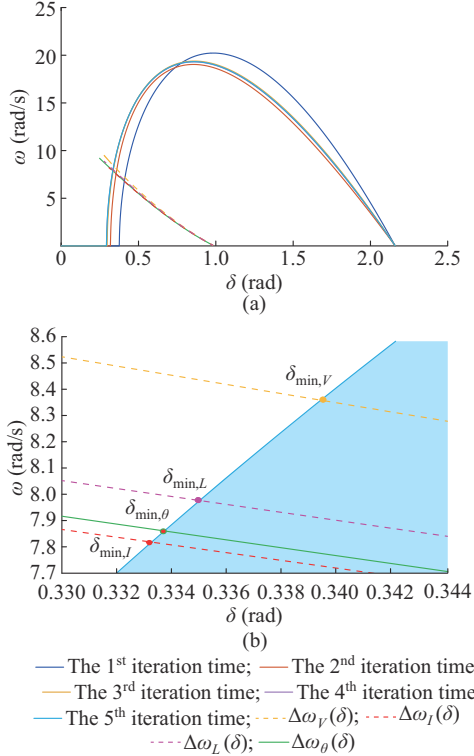


Fig. 6. Stable boundary considering post-disturbance frequency jump. (a) Zoom out. (b) Zoom in.

The intersection of $\Delta\omega_k(\delta)$ and $\omega(\delta)$ is the lower stable boundary estimated under the corresponding perturbation form k , denoted as $\delta_{\min,V}=0.340$ rad, $\delta_{\min,I}=0.333$ rad, $\delta_{\min,L}=0.335$ rad, and $\delta_{\min,\theta}=0.334$ rad, respectively. As Fig. 6(a) shows, 4-5 iterations are necessary before termination. According to (14)-(16), different disturbance forms have distinct mechanisms for generating post-disturbance frequency jumps, which cause the power-angle stable boundaries to differ. According to Fig. 6, stability sensitivity can be sorted as (from higher to lower): nominal voltage disturbance, line-inductance disturbance, phase disturbance, and current-reference disturbance.

D. Accuracy Comparison of Different Methods

Figure 7 compares the stable regions estimated using different large-signal stability analysis methods. The stable region estimated by the proposed method (blue-shaded domain) shows very little difference from the critical stable phase trajectory (black dashed curve). Therefore, it is considered free of conservatism. The conventional EAC method [25] (red-shaded domain) causes a misjudgment because it neglects the adverse effects of the reactive power loop dynamics and negative damping [4], [5]. Point b (1.57, 13.5) in Fig. 7 is within the stable region estimated by the conventional EAC method [25] but outside that estimated by the proposed method. The simulation shows that point b is unstable, which verifies the effectiveness of the proposed method

as compared with the conventional EAC method [25]. In practice, mistaking unstable systems for stable ones is unacceptable. The Lyapunov/Hamilton method [4], [21] (green dashed curve) is too conservative because the negative-damping region is directly abandoned. The improved EAC method (blue dashed curve) proposed in [5] partially improves the conservatism as compared with the Lyapunov/Hamilton method by estimating the maximum work done by the negative damping torque. However, the improved EAC cannot calculate the positive damping work and only partially captures the negative damping work (based on inequality scaling). Therefore, its conservatism is worse than that of the proposed iterative EAC, which fully captures both positive and negative damping. Considerable conservatism may lead to frequent operations by protective devices. In summary, unlike the conventional EAC, the proposed method does not misjudge stability and is much less conservative than all other existing methods, showing remarkable practical value. Table II presents the advantages and disadvantages of different transient stability analysis methods.

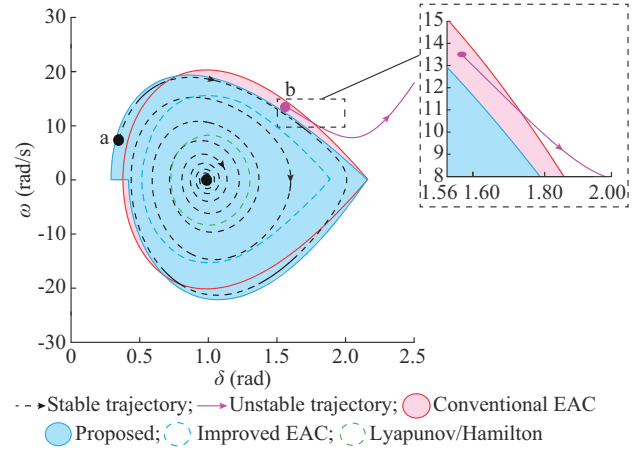


Fig. 7. Stability boundary as estimated by different methods.

TABLE II
ADVANTAGES AND DISADVANTAGES OF DIFFERENT TRANSIENT STABILITY ANALYSIS METHODS

Method	Advantage	Disadvantage
Lyapunov/Hamilton [4], [21]	Applicability for high-order systems	Difficult construction of LF, high conservatism, and ignorance of post-disturbance frequency jump
Conventional EAC [25]	Intuitiveness and simplicity	Ignorance of damping, only for 2-order systems, ignorance of post-disturbance frequency jump, and stability misjudgment
Proposed iterative EAC	Intuitive physical meaning, full capture of damping, and little conservatism	Quantity of computation
Improved EAC [5]	Partial improvement of conservatism	Damping not fully handled, ignorance of post-disturbance frequency jump, and high conservatism

IV. INTERACTION MECHANISMS BETWEEN TWO CONVERTERS AND EFFECTS OF DIFFERENT PARAMETERS

This section discusses the interaction mechanisms between

the GFL-VSC and GFM-VSC in a CIM system. The effects of different parameters on the transient stable boundary of the system are quantified based on the proposed stability analysis method. To establish the actual engineering application parameters, in addition to a stable boundary size, other physical constraints such as dynamic performance and available resources must also be considered. Parameter settings involve a complex multi-objective optimization process.

A. Dynamic Interaction Between GFL-VSCs and GFM-VSCs

The physical mechanisms of the interaction between GFL-VSCs and GFM-VSCs are revealed corresponding to (12).

1) The reactive droop loop leads to a decrease in the output voltage amplitude V_{FM} of GFM-VSC, which reduces the output capacity of the active power and increases the risk of a power imbalance between the AC-DC sides in the GFL-VSC. When the maximum output capacity of the active power is less than that of the DC-side power supply, the system becomes unstable. This interaction characteristic corresponds to the decrease in equivalent electromagnetic power $k_2 \sin \delta$ due to voltage decrease derived from the reactive droop control in (11).

2) The P - ω controller of GFM-VSC changes the frequency at the load, leading to a change in voltage of the d axis at the PCC. Thus, the active power of GFL-VSC changes with ΔP_{FL} :

$$\Delta P_{\text{FL}} = L_{\text{g}} I_{\text{FL}}^2 \cos^2 \varphi m_{\text{p}} (P_{\text{Load}} - 1.5 V_{\text{FM}} I_{\text{ref}} \cos(\delta + \varphi)) \quad (24)$$

The first term in (24) increases the output active power of the GFL-VSC by $1.5 L_{\text{g}} I_{\text{ref}}^2 \cos^2 \varphi m_{\text{p}} P_{\text{Load}}$, which is conducive to balancing the AC-DC power difference and system stability and corresponds to a decrease in equivalent mechanical power k_1 in (13). The second term in (24) reduces the output capacity of the active power of the GFL-VSC by $1.5 L_{\text{g}} I_{\text{ref}}^3 \cdot m_{\text{p}} V_{\text{FM}} \cos^2 \varphi \cos(\delta + \varphi)$, which corresponds to the $k_3 \cos \delta$ and $k_2 \sin \delta$ terms derived from the active droop controller. When $\delta + \varphi < \pi/2$, this term is positive and the output capacity of active power of the GFL-VSC is weakened, which is not favorable for stability. When $\delta + \varphi > \pi/2$, this term is negative and the output capacity of the active power of the GFL-VSC is enhanced, which enhances stability. As (25) shows, this term is overall unfavorable for the transient stability of the system:

$$\begin{cases} \int_{\delta_{\min}}^{\delta_{\max}} A \cos(\delta + \varphi) d\delta > \int_{\delta_e}^{\pi - \delta_e - 2\varphi} A \cos(\delta + \varphi) d\delta = 0 \\ A = 1.5 L_{\text{g}} I_{\text{ref}}^2 m_{\text{p}} V_{\text{FM}} \cos^2 \varphi \end{cases} \quad (25)$$

3) During the right oscillating process after disturbance, δ continues to increase, which causes $P_{\text{FL}} = 1.5 V_{\text{FM}} \cdot I_{\text{ref}} \cos(\delta + \varphi) + 1.5 I_{\text{ref}}^2 R_{\text{g}}$ to decrease. Therefore, $P_{\text{FM}} = P_{\text{Load}} - P_{\text{FL}}$ increases and causes a decrease in ω_{FM} , which further increases the relative velocity between the GFM-VSCs and GFL-VSCs and worsens stability. During the left oscillating process, δ continues to decrease, which causes P_{FL} to increase and P_{FM} to decrease. Therefore, ω_{FM} increases, which also increases the relative velocity and worsens stability. In other words, the relative frequency $\omega = \omega_{\text{PLL}} - \omega_{\text{FM}}$ changes with $1.5 m_{\text{p}} V_{\text{FM}} I_{\text{ref}} \cos(\delta + \varphi)$ and is equivalent to changes in

the relative acceleration $\ddot{\delta}$ with $-1.5 m_{\text{p}} V_{\text{FM}} I_{\text{ref}} \omega \sin(\delta + \varphi)$, which corresponds to the damping terms $k_6 \omega \sin \delta$ and $k_5 \omega \cos \delta$ in (12).

4) At the moment of current disturbance, the output power P_{FL} of the GFL-VSC increases abruptly, which causes an abrupt decrease in P_{FM} . Consequently, ω_{FM} increases abruptly due to the active droop controller, and the frequency difference between the GFL-VSC and GFM-VSC decreases abruptly, which is favorable to stability. This corresponds to the reduction of $\Delta \omega$ caused by $\Delta \omega_{\text{FM}}$ in (14).

B. Effects of Parameters on Stable Domain

1) Effects of I_{ref} and V_{N}

From (13), we can see that an increase in I_{ref} results in an increase in k_1 , which leads to a smaller maximum decelerating area with a larger δ_{e} and smaller δ_{max} . In addition, a larger I_{ref} leads to a smaller k_4 . This in turn results in lower damping and poor stability. Figure 8(a) shows the stable domains with different I_{ref} , which are consistent with the previous analysis. The increase in the nominal voltage V_{N} of the GFM-VSC leads to a larger $\sqrt{k_2^2 + k_3^2}$, which benefits transient stability because the maximum decelerating area increases. Figure 8(b) shows the stable domains with different values of V_{N} , which are consistent with the previous analysis.

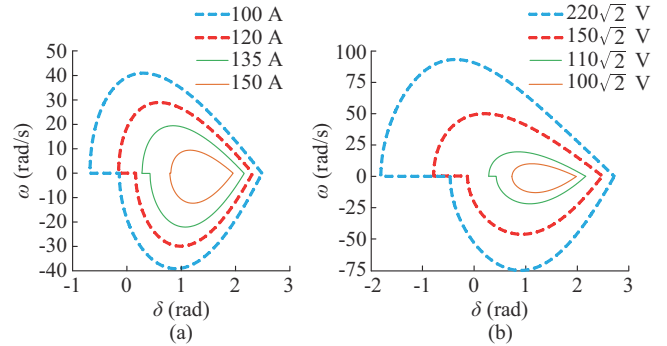


Fig. 8. Stability domain comparison. (a) Different I_{ref} . (b) Different V_{N} .

2) Effects of PI Coefficients of PLL

A larger K_{p} results in a larger k_5 , which indicates more positive damping and is favorable for stability. A larger K_{i} results in a smaller k_4 , indicating less positive damping and poorer stability. Neither K_{p} or K_{i} affects the upper boundary, which can be derived from (7) and (12). The stable domains under different K_{p} and K_{i} values obtained by the proposed iterative EAC method are compared in Fig. 9(a) and (b), which show the same trend as in the theoretical analysis. However, K_{p} cannot be so large that it results in a negative M , and thus there is no guarantee of small-signal static stability or large-signal transient stability.

3) Effects of Droop Coefficients of GFM-VSC

From (13), we can infer that the increase of m_{p} leads to a decrease in k_1 and an increase in $k_3 \cos \delta_{\text{max}}$ because $\cos \delta_{\text{max}} < 0$. Therefore, a larger m_{p} leads to a larger δ_{max} and smaller δ_{min} . From (11), we can determine that an increase in n_{q} is equivalent to a decrease in the nominal voltage V_{N} . Consequently, a larger n_{q} adversely affects stability, which is opposite the effect of V_{N} .

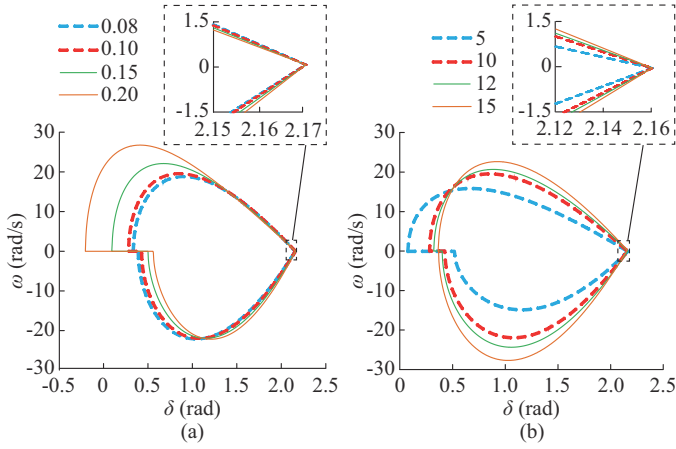


Fig. 9. Stable domain comparison. (a) Different K_p . (b) Different K_r .

The stable domains estimated by the proposed method under different m_p and n_q are shown in Fig. 10, which exhibit the same trend as in the previous analysis. In addition, ignoring the adverse effects of the reactive power loop is equivalent to assuming $n_q=0$. Therefore, the stable domains in [4] and [5] are too large, which may lead to the risk of stability misjudgment. However, a miscalculation does not occur because the improved EAC and Hamilton methods themselves are still quite conservative due to the incomplete assessment of the varying damping.

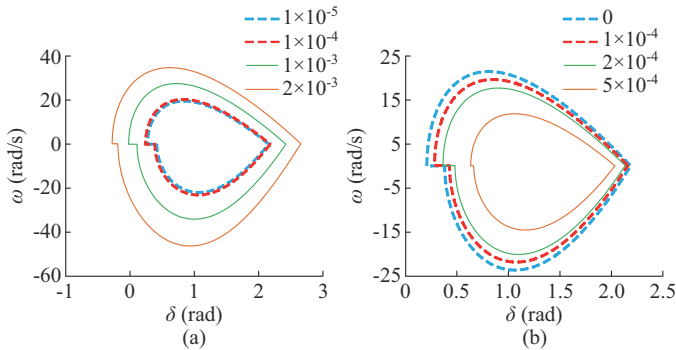


Fig. 10. Stable domain comparison. (a) Different m_p . (b) Different n_q .

4) Effects of Load and Line Parameters $P_{Load}+jQ_{Load}$ and L_g

We can infer from (13) that a smaller P_{Load} results in a larger k_1 , which deteriorates stability because it decreases the size of the decelerating area. According to (11), a larger Q_{Load} is equivalent to an increase in n_q and thus weakens stability. A larger L_g leads to a larger k_1 and smaller k_4 , which results in a smaller maximum decelerating area and more negative damping, both of which have negative effects on stability. Figure 11(a) and (b) shows estimations of the stable domains under different values of P_{Load} and L_g , respectively, where the same trend is shown as in the previous analysis. To make the trend more obvious, m_p in Fig. 11(a) is changed to be 10^{-4} .

V. SIMULATION AND EXPERIMENTAL VERIFICATION

Simulations on MATLAB/Simulink and hardware-in-loop (HIL) experiments under different types of disturbances have

been performed to prove the accuracy and low conservatism of the proposed method. The verifications are conducted by adding disturbances to I_{refd} of the GFL-VSC and V_N of the GFM-VSC, which simulate the perturbation from the DC sides of the VSCs.

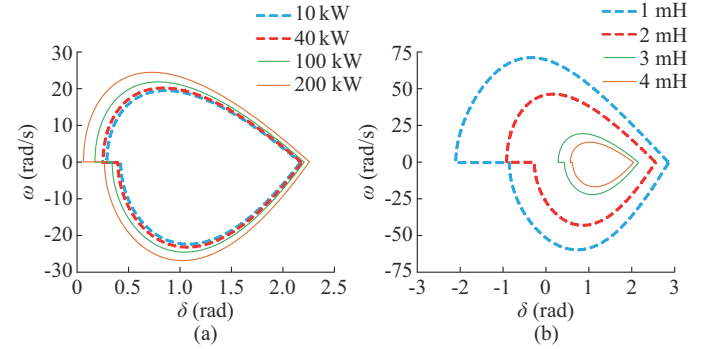


Fig. 11. Stable region comparison. (a) Different P_{Load} . (b) Different L_g .

A. Simulation Verification

1) Under-current Disturbances

The equilibrium point of the analyzed system is calculated as $\delta_e=0.984$ rad. The upper and lower stability boundaries under current disturbances as derived from the proposed method are $\delta_{min,I}=0.333$ rad and $\delta_{max}=2.160$ rad, respectively. The critical current disturbance is calculated as $\Delta I=81.21$ A. As Fig. 12(a) shows, after a small current disturbance ($\Delta I_{sma}=79$ A), the trajectories of the system are always within the stable domain and finally returned to δ_e . As Fig. 12(b) shows, the states of the system exceed the stable domain and finally lose stability after a large disturbance ($\Delta I_{lar}=82$ A). Simulation results show that the iterative EAC is effective and accurate.

2) Under Voltage Disturbances

The stable boundaries under voltage disturbance are calculated as $\delta_{min,V}=0.340$ rad and $\delta_{max}=2.160$ rad. The critical voltage disturbance is calculated as $\Delta V=229.4$ V. After a small voltage disturbance ($\Delta V_{sma}=214.4$ V), the system is always within the stable boundary and finally returned to δ_e , as shown in Fig. 13(a). However, the system exceeds the boundary and eventually loses stability after a large voltage disturbance ($\Delta V_{lar}=234.4$ V), as shown in Fig. 13(b). I_{FLa} is the a-phase output current of GFL-VSC. Simulation results demonstrate the high accuracy of the iterative EAC.

B. Experimental Verification

HIL experiments are conducted using the RT-Lab platform to verify the proposed method. The test rig for HIL experiment, which includes an RT-Lab real-time simulator, digital signal processor (DSP), and oscilloscope, is shown in Appendix A Fig. A1. The main circuit of the CIM is in the RT-Lab, whereas the controllers are implemented in the DSP. The system can remain stable when encountering disturbances within the obtained stable boundaries, as shown in Figs. 14(a) and 15(a), where $\Delta I=78$ A and $\Delta V=214.4$ V. Otherwise, the system loses stability, as shown in Figs. 14(b) and 15(b), where $\Delta I=82$ A and $\Delta V=234.4$ V.

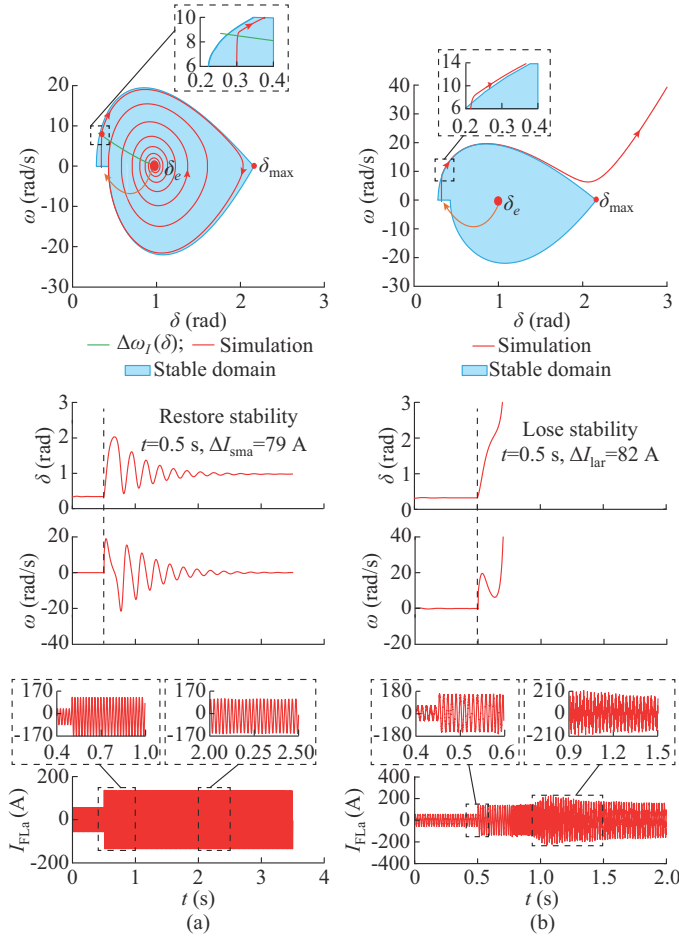


Fig. 12. Simulation under different current disturbances. (a) Stable. (b) Unstable.

VI. FURTHER DISCUSSION

The various nonlinear (nonpositive definite) damping and interactive damping terms generated by different control methods in power electronic equipment make it difficult to assess the synchronization stability of converter-based power systems. The proposed iterative EAC method innovatively accurately estimates the work of nonlinear damping through iterative calculations. Therefore, future work will utilize the basic ideas of iterative EAC and expand it to more complex converter-based power systems. This section briefly discusses the high scalability and inspirational value of the proposed method for further studies on converter-based power systems.

The transient stability of a VSG-based GFM-VSC (or low-inertia synchronous generator) and a PLL-based GFL-VSC parallel system (defined as a VSG-PLL parallel system, as shown in Fig. 16) is worth investigation [38]. However, previous studies have been mainly based on the constant-impedance model [38], [39], which ignores transient changes in line impedance due to variations in the current frequency. The mathematical structure of the nonlinear model derived in [38] is expressed as:

$$\begin{cases} \dot{\delta} = \omega \\ T_{eq} \dot{\omega} = a + b \sin(\delta + \varphi) - d\omega \cos \delta \end{cases} \quad (26)$$

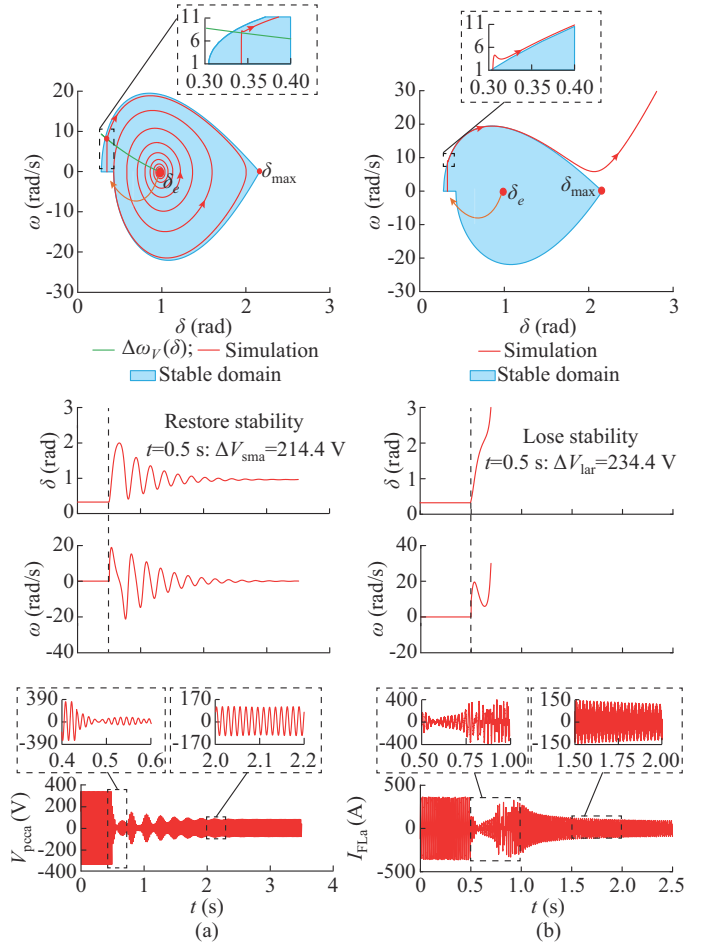


Fig. 13. Simulation under different voltage disturbances. (a) Stable. (b) Unstable.

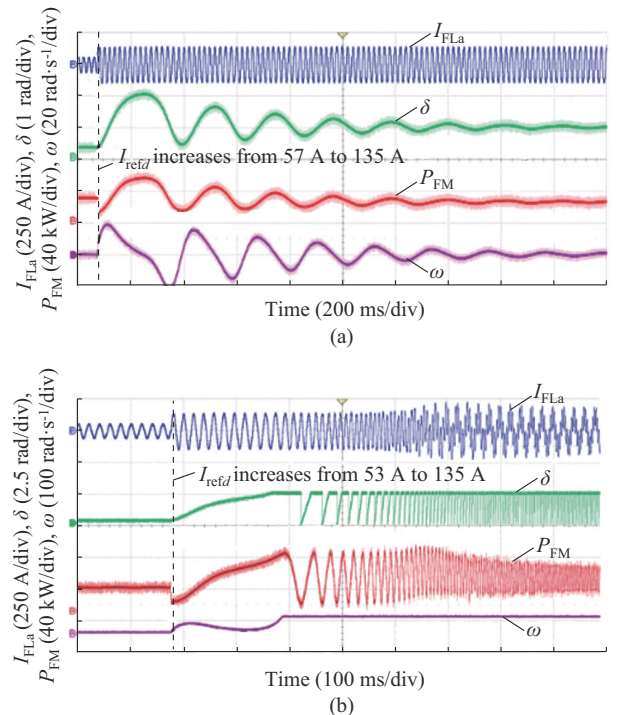


Fig. 14. Experiments under current disturbance. (a) Stable. (b) Unstable.

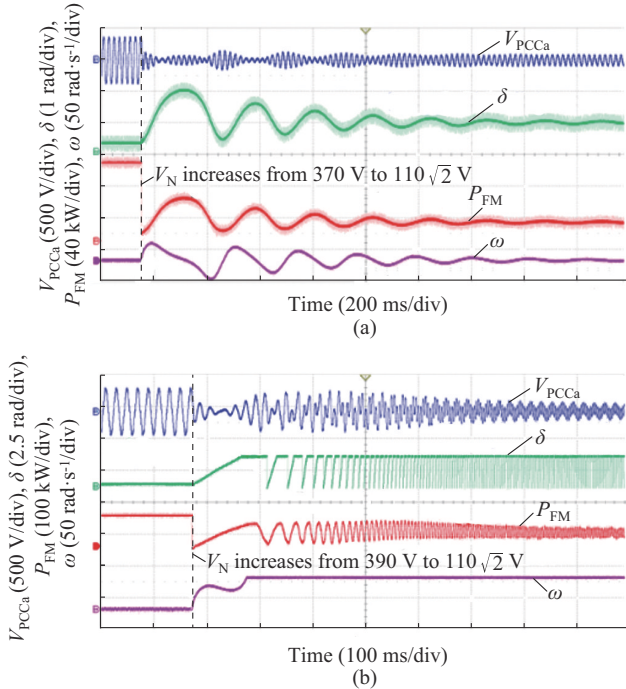


Fig. 15. Experiments under voltage disturbance. (a) Stable. (b) Unstable.

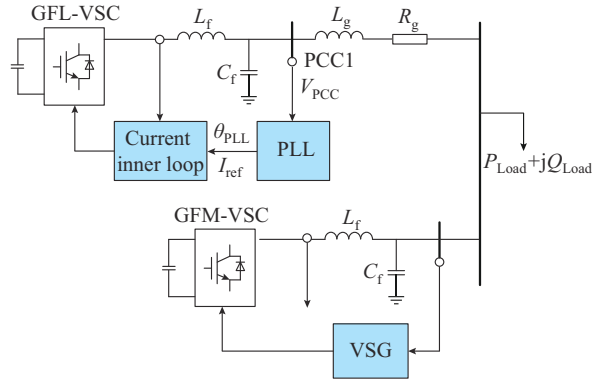


Fig. 16. Structure of VSG-PLL parallel system.

The detailed expressions of the coefficients in (26) can be found in [38] and are not repeated here. Equation (26) has a mathematical structure similar to that of (12) and an even simpler damping term. Therefore, the proposed method can be extended to the VSG-PLL parallel system and fully captures the effects of damping term $\omega \cos \delta$. However, both the theoretical derivation and simulation show that the constant impedance model leads to a smaller equivalent mechanical power and larger damping. Thus, the performance of the model in terms of stability as expressed in (26) is much better than that of the real system, and therefore, the stability analysis using the constant impedance model will misjudge the unstable system as stable, which is unacceptable in engineering applications. In addition, the stability assessment method proposed in [38] neglects the damping effects of the VSG and PLL, and therefore, its rigor requires further discussion.

The power-angle-scale nonlinear model of the VSG-PLL parallel system, which considers the change in the line im-

pedance in the transient process, can be derived as:

$$\begin{cases} \dot{\theta}_{\text{VSG}} = \omega_{\text{VSG}} \\ \dot{\omega}_{\text{VSG}} = \frac{1}{J} \left[\frac{P_{\text{ref}}}{\omega_n} - \frac{P_{\text{Load}} - 1.5V_{\text{FM}}I_{\text{ref}} \cos(\theta_{\text{PLL}} - \theta_{\text{VSG}} + \varphi)}{\omega_n} - D_p(\omega_{\text{VSG}} - \omega_n) \right] \\ \dot{\theta}_{\text{PLL}} = \omega_{\text{PLL}} \\ \dot{\omega}_{\text{PLL}} = K_p [V_{\text{FM}} \cos(\theta_{\text{VSG}} - \theta_{\text{PLL}})(\omega_{\text{VSG}} - \omega_{\text{PLL}}) + \dot{\omega}_{\text{PLL}} L_g I_{\text{ref}} \cos \varphi] + K_i [V_{\text{FM}} \sin(\theta_{\text{VSG}} - \theta_{\text{PLL}}) + \dot{\theta}_{\text{PLL}} L_g I_{\text{ref}} \cos \varphi + I_{\text{ref}} R_g \sin \varphi] \end{cases} \quad (27)$$

where P_{ref} , θ_{VSG} , and ω_{VSG} are the active power reference, output voltage phase, and frequency of VSG, respectively; and J and D_p are the virtual inertia and virtual damping of VSG, respectively.

The dynamics and stability of (27) cannot be directly analyzed using the phase and frequency differences between the two VSCs. The damping effects in (27) can be analyzed using the iterative EAC. However, accurate transient stability analysis presents another difficulty, i. e., interaction terms. Most previous studies have only qualitatively analyzed or conservatively estimated the effects of interaction terms, but failed to perform accurate calculations [28]. In further studies, we will combine mathematical scaling with the proposed method to obtain a stable domain estimation of a VSG-PLL parallel system with the minimal conservatism.

VII. CONCLUSION

In this paper, we investigate the transient stability of a CIM system considering the post-disturbance frequency jump phenomena in the PLL and droop controller and the coupling interaction between the active and reactive droop controllers. An iterative EAC has been proposed to provide an assessment of transient stability under varying damping that is free of conservatism. In addition, the dynamic interaction mechanisms between the GFL-VSCs and GFM-VSCs and the effects of the parameters on stability have been analyzed. The proposed iterative EAC does not have a misjudgment risk and shows much less conservatism than existing methods. Further discussion demonstrate that the proposed method has high scalability. The main conclusions are as follows.

1) At the moment of disturbance, both GFL-VSCs and GFM-VSCs may behave with a post-disturbance frequency jump, which produces large signal model errors in the initial values and may lead to stability misjudgment.

2) The effects of the reactive power loop dynamics by the varying damping are accurately calculated.

3) The interaction between the GFM-VSCs and GFL-VSCs is complex, and some interactions deteriorate the stability, whereas others are beneficial.

4) A larger nominal voltage, active droop coefficient, active load, and PLL proportional coefficient are conducive to transient stability. By contrast, a larger current reference,

line inductance, reactive power droop coefficient, reactive load, and PLL integral coefficient deteriorate the stability.

APPENDIX A

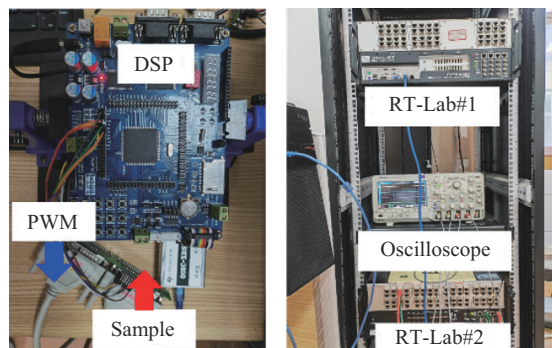


Fig. A1. RT-Lab-based test rig for HIL experiments.

REFERENCES

- [1] M. Farrokhbadi, C. Cañizares, J. Simpson-Porco *et al.*, “Microgrid stability definitions, analysis, and examples,” *IEEE Transactions on Power Systems*, vol. 35, no. 1, pp. 13-29, Jan. 2020.
- [2] Q. Zhou, Z. Tian, M. Shahidehpour *et al.*, “Optimal consensus-based distributed control strategy for coordinated operation of networked microgrids,” *IEEE Transactions on Power Systems*, vol. 35, no. 3, pp. 2452-2462, May 2020.
- [3] I. Subotić, D. Groß, M. Colombino *et al.*, “A Lyapunov framework for nested dynamical systems on multiple time scales with application to converter-based power systems,” *IEEE Transactions on Automatic Control*, vol. 66, no. 12, pp. 5909-5924, Dec. 2021.
- [4] Z. Tian, X. Li, X. Zha *et al.*, “Transient synchronization stability of an islanded AC microgrid considering interactions between grid-forming and grid-following converters,” *IEEE Journal of Emerging and Selected Topics in Power Electronics*, vol. 11, no. 4, pp. 4463-4476, Aug. 2023.
- [5] Y. Tang, Z. Tian, X. Zha *et al.*, “An improved equal area criterion for transient stability analysis of converter-based microgrid considering nonlinear damping effect,” *IEEE Transactions on Power Electronics*, vol. 37, no. 9, pp. 11272-11284, Sept. 2022.
- [6] J. Rocabert, A. Luna, F. Blaabjerg *et al.*, “Control of power converters in AC microgrids,” *IEEE Transactions on Power Electronics*, vol. 27, no. 11, pp. 4734-4749, Nov. 2012.
- [7] A. Tayyebi, D. Groß, A. Anta *et al.*, “Frequency stability of synchronous machines and grid-forming power converters,” *IEEE Journal of Emerging and Selected Topics in Power Electronics*, vol. 8, no. 2, pp. 1004-1018, Jun. 2020.
- [8] M. A. Awal and I. Husain, “Unified virtual oscillator control for grid-forming and grid-following converters,” *IEEE Journal of Emerging and Selected Topics in Power Electronics*, vol. 9, no. 4, pp. 4573-4586, Aug. 2021.
- [9] L. Zhang, L. Harnefors, and H.-P. Nee, “Power-synchronization control of grid-connected voltage-source converters,” *IEEE Transactions on Power Systems*, vol. 25, no. 2, pp. 809-820, May 2010.
- [10] J. Matevosyan, B. Badrzadeh, T. Prevost *et al.*, “Grid-forming inverters: are they the key for high renewable penetration?” *IEEE Power and Energy Magazine*, vol. 21, no. 2, pp. 77-86, Mar.-Apr. 2023.
- [11] J. Matevosyan, J. MacDowell, N. Miller *et al.*, “A future with inverter-based resources: finding strength from traditional weakness,” *IEEE Power and Energy Magazine*, vol. 19, no. 6, pp. 18-28, Nov.-Dec. 2021.
- [12] P. Yu, X. Zha, Z. Tian *et al.*, “Frequency-dependent network analysis and stability enhanced design for voltage-source converters under weak grid conditions,” *IEEE Transactions on Power Delivery*, vol. 37, no. 6, pp. 4593-4602, Dec. 2022.
- [13] D. Pattabiraman, R. H. Lassete, and T. M. Jahns, “Impact of phase-locked loop control on the stability of a high inverter penetration power system,” in *Proceedings of 2019 IEEE PES General Meeting*, Atlanta, USA, Aug. 2019, pp. 1-5.
- [14] M. G. Taul, X. Wang, P. Davari *et al.*, “An overview of assessment methods for synchronization stability of grid-connected converters under severe symmetrical grid faults,” *IEEE Transactions on Power Electronics*, vol. 34, no. 10, pp. 9655-9670, Oct. 2019.
- [15] H. Geng, L. Liu, and R. Li, “Synchronization and reactive current support of PMSG-based wind farm during severe grid fault,” *IEEE Transactions on Sustainable Energy*, vol. 9, no. 4, pp. 1596-1604, Oct. 2018.
- [16] C. Yang, L. Huang, H. Xin *et al.*, “Placing grid-forming converters to enhance small signal stability of PLL-integrated power systems,” *IEEE Transactions on Power Systems*, vol. 36, no. 4, pp. 3563-3573, Jul. 2021.
- [17] Y. Zhang, C. Zhang, and X. Cai, “Large-signal grid-synchronization stability analysis of PLL-based VSCs using Lyapunov’s direct method,” *IEEE Transactions on Power Systems*, vol. 37, no. 1, pp. 788-791, Jan. 2022.
- [18] M. Kabalan, P. Singh, and D. Niebur, “Large signal Lyapunov-based stability studies in microgrids: a review,” *IEEE Transactions on Smart Grid*, vol. 8, no. 5, pp. 2287-2295, Sept. 2017.
- [19] C. Zhang, M. Molinas, Z. Li *et al.*, “Synchronizing stability analysis and region of attraction estimation of grid-feeding VSCs using sum-of-squares programming,” *Frontiers in Energy Research*, vol. 8, p. 56, Apr. 2020.
- [20] H. Cheng, Z. Shuai, C. Shen *et al.*, “Transient angle stability of paralleled synchronous and virtual synchronous generators in islanded microgrids,” *IEEE Transactions on Power Electronics*, vol. 35, no. 8, pp. 8751-8765, Aug. 2020.
- [21] X. Fu, J. Sun, M. Huang *et al.*, “Large-signal stability of grid-forming and grid-following controls in voltage source converter: a comparative study,” *IEEE Transactions on Power Electronics*, vol. 36, no. 7, pp. 7832-7840, Jul. 2021.
- [22] Z. Tian, Y. Tang, X. Zha *et al.*, “Hamilton-based stability criterion and attraction region estimation for grid-tied inverters under large-signal disturbances,” *IEEE Journal of Emerging and Selected Topics in Power Electronics*, vol. 10, no. 1, pp. 413-423, Feb. 2022.
- [23] J. Zhao, M. Huang, and X. Zha, “Transient stability analysis of grid-connected VSIs via PLL interaction,” in *Proceedings of 2018 IEEE International Power Electronics and Application Conference and Exposition (PEAC)*, Shenzhen, China, Nov. 2018, pp. 1-6.
- [24] D. Pan, X. Wang, F. Liu *et al.*, “Transient stability impact of reactive power control on grid-connected converters,” in *Proceedings of 2019 IEEE Energy Conversion Congress and Exposition (ECCE)*, Baltimore, USA, Sept.-Oct. 2019, pp. 4311-4316.
- [25] Q. Hu, L. Fu, F. Ma *et al.*, “Large signal synchronizing instability of PLL-based VSC connected to weak AC grid,” *IEEE Transactions on Power Systems*, vol. 34, no. 4, pp. 3220-3229, Jul. 2019.
- [26] L. Xiong, F. Zhou, F. Wang *et al.*, “Static synchronous generator model: a new perspective to investigate dynamic characteristics and stability issues of grid-tied PWM inverter,” *IEEE Transactions on Power Electronics*, vol. 31, no. 9, pp. 6264-6280, Sept. 2016.
- [27] X. He, H. Geng, J. Xi *et al.*, “Resynchronization analysis and improvement of grid-connected VSCs during grid faults,” *IEEE Journal of Emerging and Selected Topics in Power Electronics*, vol. 9, no. 1, pp. 438-450, Feb. 2021.
- [28] X. Fu, M. Huang, S. Pan *et al.*, “Cascading synchronization instability in multi-VSC grid-connected system,” *IEEE Transactions on Power Electronics*, vol. 37, no. 7, pp. 7572-7576, Jul. 2022.
- [29] X. He and H. Geng, “PLL synchronization stability of grid-connected multiconverter systems,” *IEEE Transactions on Industry Applications*, vol. 58, no. 1, pp. 830-842, Jan.-Feb. 2022.
- [30] X. Li, Z. Tian, X. Zha *et al.*, “An iterative equal area criterion for transient stability analysis of grid-tied converter systems with varying damping,” *IEEE Transactions on Power Systems*, vol. 39, no. 1, pp. 1771-1784, Jan. 2024.
- [31] X. Huang, K. Wang, J. Qiu *et al.*, “Decentralized control of multi-parallel grid-forming DGs in islanded microgrids for enhanced transient performance,” *IEEE Access*, vol. 7, pp. 17958-17968, Jan. 2019.
- [32] Y. Tang, Y. Hu, Z. Tian *et al.*, “Transient stability analysis for grid-tied virtual synchronous generator based on T-S fuzzy modeling and LMI approach,” in *Proceedings of 2021 IEEE 5th Conference on Energy Internet and Energy System Integration (EI2)*, Taiyuan, China, Oct. 2021, pp. 2730-2736.
- [33] Z. Shuai, C. Shen, X. Liu *et al.*, “Transient angle stability of virtual synchronous generators using Lyapunov’s direct method,” *IEEE Transactions on Smart Grid*, vol. 10, no. 4, pp. 4648-4661, Jul. 2019.
- [34] M. Li, X. Quan, Z. Wu *et al.*, “Modeling and transient stability analysis of mixed-GFM-GFL-based power system,” in *Proceedings of 2021 IEEE Sustainable Power and Energy Conference (ISPEC)*, Nanjing, China, Dec. 2021, pp. 2755-2759.
- [35] S. Liao, X. Zha, X. Li *et al.*, “A novel dynamic aggregation modeling

method of grid-connected inverters: application in small-signal analysis," *IEEE Transactions on Sustainable Energy*, vol. 10, no. 3, pp. 1554-1564, Jul. 2019.

- [36] X. Zha, S. Liao, M. Huang *et al.*, "Dynamic aggregation modeling of grid-connected inverters using Hamilton's-action-based coherent equivalence," *IEEE Transactions on Industrial Electronics*, vol. 66, no. 8, pp. 6437-6448, Aug. 2019.
- [37] X. Li, Z. Tian, X. Zha *et al.*, "Nonlinear modeling and stability analysis of grid-tied paralleled-converter systems based on the proposed dual-iterative equal area criterion," *IEEE Transactions on Power Electronics*, vol. 38, no. 6, pp. 7746-7759, Jun. 2023.
- [38] C. He, X. He, H. Geng *et al.*, "Transient stability of low-inertia power systems with inverter-based generation," *IEEE Transactions on Energy Conversion*, vol. 37, no. 4, pp. 2903-2912, Dec. 2022.
- [39] S. P. Me, M. H. Ravanji, M. Z. Mansour *et al.*, "Transient stability of paralleled virtual synchronous generator and grid-following inverter," *IEEE Transactions on Smart Grid*, vol. 14, no. 6, pp. 4451-4466, Nov. 2023.

Xilin Li received the B.Eng. degree (major in electrical engineering and minor in computer science and technology) from Wuhan University, Wuhan, China, in 2021, where he is currently working toward the Ph.D. degree in electrical engineering. His research interests include control and transient stability analysis of converter-based power systems.

Jingyi Zhang received the B.Eng. degree in electrical engineering from Northwestern Polytechnical University, Xi'an, China, in 2022. She is currently working toward the M.Eng. degree in electrical engineering at Wuhan University, Wuhan, China. Her research interests include control and stability of voltage source converter-based high-voltage direct current (VSC-HVDC) systems.

Zhen Tian received the B.S. degree in electrical engineering from Wuhan University, Wuhan, China, in 2014, and the Ph.D. degree in control science and engineering from Shanghai Jiao Tong University, Shanghai, China, in 2019. During 2017-2019, he was a Visiting Scholar with the Department of Electrical and Computer Engineering, Illinois Institute of Technology, Chicago, USA. He was a Postdoctoral Fellow with the School of Electrical Engineering and Automation, Wuhan University, where he has been an Associate

Research Fellow since 2022. His research interests mainly include modeling, control, and stability analysis of renewable energy generation, microgrids, and power-electronics-enabled power systems.

Xiaoming Zha received B.S., M.S., and Ph.D. degrees in electrical engineering from Wuhan University, Wuhan, China, in 1989, 1992, and 2001, respectively. He was a Postdoctoral Fellow at the University of Alberta, Edmonton, Canada, from 2001 to 2003. He has been a Faculty Member of Wuhan University since 1992, and became a Professor in 2003. His research interests include power electronic converters, application of power electronics in smart grid and renewable energy generation, analysis and control of microgrids, analysis and control of power quality, and frequency control of high-voltage high-power electric motors.

Wei Wang received the M.S. degree from the Electric Power Automation Research Institute, Nanjing, China, in 2000, and the Ph.D. degree in electrical engineering from Harbin Institute of Technology, Harbin, China, in 2013. Since 2018, he has been the Vice President and Chief Engineer of NARI Research Institute, NARI Technology Co., Ltd., Nanjing, China. He is a Researcher-level Senior Engineer, a Vice Chairman of the Energy Storage Equipment Special Committee of IEEE PES China Technical Committee, and a Member of the National Wind Machinery Standardization Committee. His research interests include excitation control of large generator sets, power electronic converter technology, grid-connected operation, and control technology of renewable energy power generation.

Meng Huang received the B.Eng. and M.Eng. degrees from Huazhong University of Science and Technology, Wuhan, China, in 2006 and 2008, respectively, and the Ph.D. degree from the Hong Kong Polytechnic University, Hong Kong, China, in 2013, all in electrical engineering. He is currently a Professor with the School of Electrical Engineering and Automation, Wuhan University, Wuhan, China. His research interests include safe operation and control of grid-connected systems.

Chong Shao received the B.S. and Ph.D. degrees in electrical engineering from Tsinghua University, Beijing, China, in 2006 and 2011, respectively. He is currently the Director of the Grid Control Center in State Grid Gansu Electric Power Company, Lanzhou, China. His research interests include operation, modeling, and analysis of renewable energy-integrated power system.